Palaeogeography, Palaeoclimatology, Palaeoecology 647 (2024) 112234

Contents lists available at ScienceDirect

Palaeogeography, Palaeoclimatology, Palaeoecology

journal homepage: www.elsevier.com/locate/palaeo

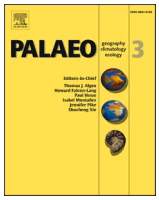

Paleoenvironment reconstruction of the eastern Tethys during the pre-onset excursion preceding the PETM

Yixin Dong [a,b], Anthony Gachetti [b], Qingting Wu [b], Maurizia De Palma [b], Xiumian Hu [c], Stefanie Brachfeld [b], Zhilin Yang [d], Jiuyuan Wang [e], Yasu Wang [f], Shijun Jiang [f], Ying Cui [b,*]

[a] State Key Laboratory of Oil and Gas Reservoir Geology and Exploitation, Chengdu University of Technology, Chengdu 610059, China
[b] Department of Earth and Environmental Studies, Montclair State University, NJ 07043, United States of America
[c] State Key Laboratory of Mineral Deposit Research, School of Earth Sciences and Engineering, Nanjing University, Nanjing 210023, China
[d] Exploration and Development Research Institute, Tarim Oilfield Company, PetroChina, Korla 841000, Xinjiang, China
[e] School of Earth and Space Sciences, Peking University, Beijing 100871, China
[f] College of Oceanography, Hohai University, Nanjing 245700, China

ARTICLE INFO

Editor: Howard Falcon-Lang

Keywords:
Pre-onset Excursion
Eastern Tethys
Paleoenvironment
Trace element geochemistry
Magnetic susceptibility

ABSTRACT

A rapid warming event known as the pre-onset excursion (POE) occurred prior to the Paleocene-Eocene Thermal Maximum (PETM). It is less well studied compared to the PETM due to the limited number of well-resolved records globally despite its importance in shaping the subsequent PETM. Shallow marine environments, particularly in low latitudes, are insufficiently documented despite their significant influence on heat and moisture distribution. Here we report high temporal resolution geochemical and magnetic susceptibility records from a well-preserved shallow marine Kuzigongsu section in the Tarim Basin in China to reconstruct the paleoenvironment of the eastern Tethys during the POE. Changes in chemical weathering proxies (*e.g.*, chemical index of alteration [CIA] and Rb/Sr) suggest chemical weathering intensification occurred after the POE. Higher enrichment factors of P, Ba, Ni, and Cu support increased primary productivity due to enhanced river runoff and nutrient input, which aligns with the observed rise in magnetic susceptibility. Concurrently, the eastern Tethys experienced bottom water deoxygenation, which is supported by redox-sensitive proxies (*e.g.*, elevated enrichment factors of U and V, and low Mn* values). Increased $\delta^{15}N_{org}$ values provide additional evidence of enhanced reduction processes due to increased productivity, attributed to enhanced denitrification and ^{15}N enrichment in seawater's NO_3^- reservoir. The carbon isotope excursion during the POE recovers significantly faster than that during the PETM yet coincides with lingering environmental impacts that are also globally reported for the PETM. These paleoenvironmental proxies reflect notable changes in chemical weathering, ocean productivity, and redox conditions of the eastern Tethys region, potentially setting the stage for the anomalously impactful PETM.

1. Introduction

The Paleocene-Eocene Thermal Maximum (PETM; ~56 Ma) was preceded by a rapid precursory sub-Milankovitch global warming event recognized as the pre-onset excursion (POE) (Babila et al., 2022). The POE is characterized by a small yet significant carbon isotope excursion (CIE) of ~2 to 3‰ (Babila et al., 2022; Bowen et al., 2015; Doubrawa et al., 2022; Sluijs et al., 2007), which is smaller than that of the PETM (~ 3 to 6‰; McInerney and Wing, 2011). The driver of the POE remains debated, but possible ^{13}C-depleted carbon sources include volcanic CO_2 emissions from the emplacement of the North Atlantic Igneous Province (NAIP) (Jones et al., 2019) and methane release (Babila et al., 2022; Bowen et al., 2015). Compared to the ~5 to 10 °C global warming during the PETM (Frieling et al., 2017; Stokke et al., 2020), the increased temperature during the POE was relatively smaller, ranging from ~2 to 5 °C (Babila et al., 2022; Doubrawa et al., 2022). Additionally, the duration of the POE may have spanned a few hundred years to millennia (Babila et al., 2022; Bowen et al., 2015; Doubrawa et al., 2022), shorter than the PETM, which lasted approximately 150 to 220 kyr (Aziz et al., 2008; Westerhold et al., 2018; Zachos et al., 2005). Extreme global warming during the PETM resulted in significant environmental changes, including intensified tropical cyclones (Kiehl et al.,

* Corresponding author.
E-mail address: cuiy@montclair.edu (Y. Cui).

https://doi.org/10.1016/j.palaeo.2024.112234
Received 1 January 2024; Received in revised form 29 March 2024; Accepted 22 April 2024
Available online 23 April 2024

2021; Rush et al., 2021), enhanced hydrological cycles and weathering (Carmichael et al., 2018; Chen et al., 2023), sea level rise (Jiang et al., 2023; Sluijs et al., 2014), ocean acidification (Babila et al., 2016; Penman et al., 2014), ocean deoxygenation (Clarkson et al., 2021; Stramma et al., 2008), and changes in ocean circulation (Nunes and Norris, 2006). However, the understanding of the environmental response to the POE remains limited due to the lack of well-preserved POE records in the deep sea. Existing studies suggest that the POE was associated with ocean acidification, reflected by a negative shift in $\delta^{11}B$ values of benthic foraminifera (Babila et al., 2022). The POE may be a useful analogue for the ongoing anthropogenic carbon emissions due to its relatively small carbon release within a shorter amount of time (Babila et al., 2022).

Calcareous mudstones of the latest Paleocene in the western Tarim Basin of the eastern Tethys provide an archive of the global impact of the POE (Fig. 1; Wang et al., 2022; Wu et al., 2024). Here we present a comprehensive record of major and trace elements, nitrogen isotopes of bulk organic matter ($\delta^{15}N_{org}$), and magnetic susceptibility (χ) from the latest Paleocene strata of the Kuzigongsu section in the Tarim Basin, northwestern China. Our dataset facilitates the reconstruction of environmental dynamics of the eastern Tethys during the POE, including assessments of sediment provenance, chemical weathering, marine primary productivity, and redox conditions.

2. Geological settings

2.1. Regional geological background

Located within the Xinjiang Uygur Autonomous Region in northwestern China, the Tarim Basin represents the country's largest inland basin spanning 563,000 km^2. The Tarim Basin is enclosed by the Kunlun and Altun Mountains to the south, the Tian Shan Mountains to the north, and the Taklamakan Desert in the middle. Since the late Early Cretaceous (*i.e.*, the Cenomanian), seawater from the eastern Tethys Ocean infiltrated eastward through narrow passageways between the Tianshan and Kunlun Ranges, resulting in the formation of the Tarim Sea (Fig. 1B) (Bosboom et al., 2011; Xi et al., 2016; Zhang et al., 2018). Notably, the Tarim Sea underwent five significant transgressions up to the end of the Paleogene, in which the sedimentary deposits extending from the Late Paleocene to Early Eocene signify the third transgressive phase (Jiang et al., 2023; Kaya et al., 2019).

The Kuzigongsu section (39°45′10″ N, 75°17′29″ E) of this study is located in the Wuqia County within the southwestern region of the Tarim Basin. During the Late Paleocene to Early Eocene period, this area was a semi-restricted epicontinental seaway connected to the Tethys Ocean (Cao et al., 2018; Zhang et al., 2018) (Fig. 1B). The sedimentary environment during this period manifested as a marine carbonate ramp characterized by shallow water depths (Jiang et al., 2023; Kaya et al., 2019). The strata of the Kuzigongsu section consists of the Altash Formation and the Lower Qimugen Formation. The Altash Formation predominantly consists of thick layers of gypsum interspersed with dolomitic limestone beds, indicative of a sabkha sedimentary environment. The overlying Lower Qimugen Formation in conformable contact with the Altash Formation extends from the latest Paleocene to the early Eocene (Fig. 2). It comprises gray wackestone (0–9.1 m, 36.8–41.2 m, and 44.6–47.1 m), bivalve–rich bioclastic limestone (29.8–31.2 m) and gray-greenish calcareous mudstone (9.1–29.8 m, 31.2–36.8 m, and 41.2–44.6 m) (Jiang et al., 2023; Li et al., 2021; Zhang et al., 2018). The basal part of the Lower Qimugen Formation (0–19.9 m) was deposited in tidal to lagoonal environments influenced by terrigenous supply. During the PETM onset, the sedimentary environment transitioned to middle ramp settings due to rapid transgression, then progressed into outer ramp environments during the main PETM phase (Jiang et al., 2023). Since the sedimentary records of the PETM (19.9–30.5 m) have been reported elsewhere (Wang et al., 2022; Wu et al., 2024), we focus on the stratigraphic record below the PETM strata that preserves the POE, which is mainly composed of gray wackestone (0–9.1 m) and gray-greenish calcareous mudstone (9.1–19.9 m) in the Kuzigongsu section (Fig. 2).

2.2. Stable carbon isotope stratigraphy

The occurrence of the POE in the study section is grounded by the concurrent negative excursions in $\delta^{13}C_{org}$ and $\delta^{13}C_{carb}$ (Wang et al., 2022; Wu et al., 2024). The shallow marine Kuzigongsu section documents a continuous sedimentary record with moderately high sedimentation rates (~ 6.5 cm kyr^{-1}; Wu et al., 2024) (Fig. 2). The depositional age of the studied interval is considered to be within the NP9a nannofossil zone of the Late Paleocene Thanetian period, evidenced by the detailed calcareous nannofossil biostratigraphy (Wang et al., 2022). In the study interval, the $\delta^{13}C_{carb}$ and $\delta^{13}C_{org}$ values range from −1.6 to 3.1‰ and from −27.1 to −24.1‰, respectively (Table S1). The magnitudes of concurrent negative excursions of $\delta^{13}C_{carb}$ and $\delta^{13}C_{org}$ are ~ 2.0‰ and 2.6‰, respectively, followed by a rapid recovery, which allows for the identification of the POE. The stratigraphic record can be divided into pre-POE (0–10.4 m), POE (10.4–11.4 m) and post-POE (11.4–19.9 m) intervals based on the negative excursion of carbon isotopes (Fig. 2). Furthermore, the observed negative excursion

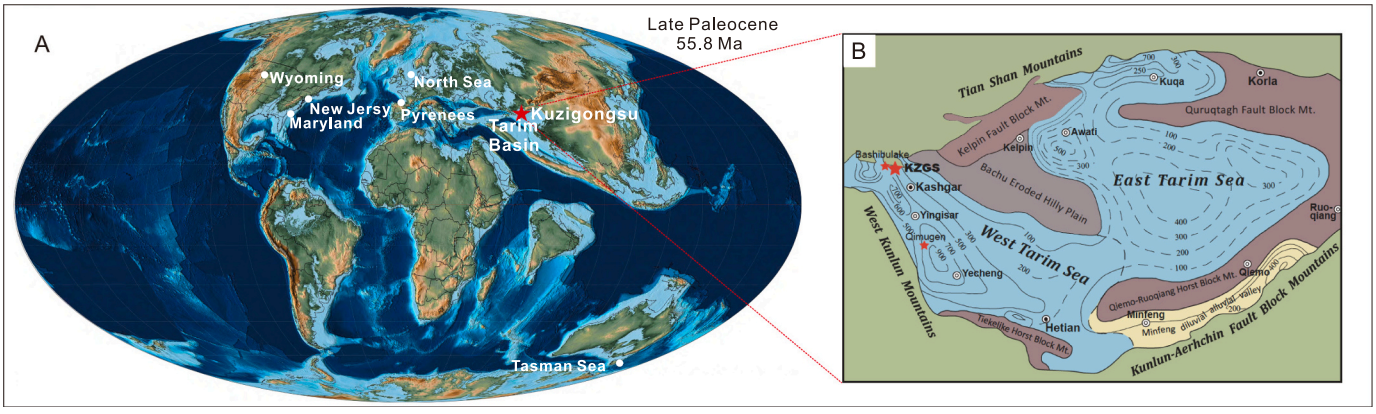

Fig. 1. A) Global paleogeography and the study location in the Late Paleocene (after Scotese, 2014); Solid white circles represent other shallow water POE records in the Maryland and New Jersey Coastal Plains regions in the United States (Babila et al., 2022; Doubrawa et al., 2022; Sluijs et al., 2007), the North Sea Basin (Kender et al., 2012), the Pyrenean foreland basins (Tremblin et al., 2022), the Tasman Sea (Elling et al., 2019), and the Bighorn Basin in Wyoming, United States (Bowen et al., 2015). B) Paleogeographic setting of the Tarim Basin and the study location shown by the large red star (after Wu et al., 2024). (For interpretation of the references to colour in this figure legend, the reader is referred to the web version of this article.)

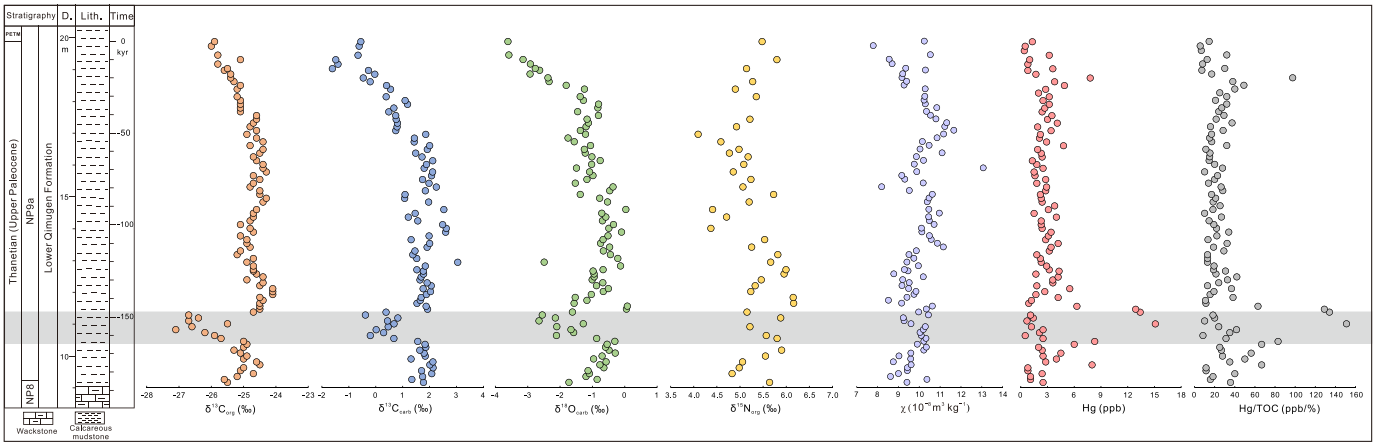

Fig. 2. Geochemical records of the study site across the POE based on prior studies and new data. The gray shaded area shows the POE interval (10.4–11.4 m). $\delta^{13}C_{carb}$ and $\delta^{18}O_{carb}$ records are from Wang et al. (2022). The $\delta^{15}N_{org}$ and magnetic susceptibility (χ) data are from this study.

in $\delta^{18}O_{carb}$ (~ −2.3‰) indicate surface ocean temperature rise, supported by the elevated Mg/Ca ratios of foraminifera observed in the Atlantic coastal plains (Babila et al., 2022).

3. Methods

3.1. Major and trace element geochemistry

A total of 96 calcareous mudstone samples were collected at an average interval of 10 cm from 9.1 to 19.8 m within the Lower Qimugen Formation in the Kuzigongsu section (Table S1). Major, trace and rare earth element data and related analytical procedures have been reported in Wu et al. (2024), which focused on the interpretation of paleoenvironmental changes during the PETM. Here, we aim to provide a detailed paleoenvironmental reconstruction of the POE using the elemental dataset from Wu et al. (2024) that includes chemical weathering, sediment provenance, and nutrient and redox conditions of the eastern Tethys.

Various chemical weathering proxies were calculated *via* molar proportions of major oxides to reconstruct the chemical weathering intensity. The most extensively used chemical weathering proxy, the Chemical Index of Alteration (CIA), was calculated from the equation $CIA = [Al_2O_3/(Al_2O_3 + CaO^* + Na_2O + K_2O)] \times 100$, which quantifies the degree of feldspar transformation to clay minerals during chemical weathering (Nesbitt and Young, 1982). It is important to note that the CaO* reflects only Ca in the silicate fraction, not the carbonate or apatite fraction of the rock, and is calculated as $CaO^* = Minimum(CaO - P_2O_5 \times 10/3, Na_2O)$ (McLennan, 1993; Panahi et al., 2000). To assess the degree of plagioclase weathering, the Plagioclase Index of Alteration was calculated with the equation $PIA = [(Al_2O_3 - K_2O)/(Al_2O_3 + CaO^* + Na_2O - K_2O)] \times 100$) (Fedo et al., 1995). Other chemical weathering proxies include the Chemical Index of Weathering ($CIW = [Al_2O_3/(Al_2O_3 + CaO^* + Na_2O)] \times 100$; Harnois, 1988), modified Chemical Index of Alteration ($CIX = [Al_2O_3/(Al_2O_3 + Na_2O + K_2O)] \times 100$; Garzanti et al., 2014), and Weathering Index of Parker ($WIP = [2Na_2O/0.35 + MgO/0.9 + 2K_2O/0.25 + CaO^*/0.7] \times 100$; Parker, 1970). Enrichment factors (EF) were calculated for trace elements with the equation $X_{EF} = [(X/Al)\ sample\ /(X/Al)_{average\ shale}]$ (Tribovillard et al., 2006), where X represents the measured concentration of the element in this study and the reported concentration of the element in the average shale from Wedepohl (1991). The concentrations of rare earth elements (REEs) were normalized to the Post-Archean Australian Shale (PAAS; Pourmand et al., 2012) to eliminate the odd-even effect. Because these proxies are most useful for mudstone, our interpretation is focused on the interval of calcareous mudstones (9.1–19.9 m) with low carbonate content (< 25 wt.%).

3.2. Magnetic susceptibility

Rock chips were analyzed for bulk mass-normalized magnetic susceptibility (χ) using an MFK2-FA Kappabridge at Montclair State University. Chips were selected with a minimum mass requirement of 1 g. Measurements were made at room temperature with an applied field amplitude of 200 A/m and frequency of 976 Hz. Each measurement is corrected for the contribution of the plastic sample holder. Each sample was measured three times, with the average value normalized by mass to obtain χ in units of $m^3\ kg^{-1}$. Relative standard deviations between the three replicates were generally <0.5%.

3.3. Nitrogen isotopes

44 homogenized bulk sediments were analyzed for nitrogen isotopes at Montclair State University using a Thermo Scientific™ EA IsoLink™ coupled to a Delta Advantage Isotope Ratio Mass Spectrometer (IRMS). ~20 mg pre–weighed samples were wrapped in tin boats and loaded into the sample carousel for isotope analysis. Samples were combusted with excess oxygen at 1008 °C in the oxidation reactor, which was filled with chromium (III) oxide and silver–plated cobalt oxide to ensure complete oxidation. The produced N_2 gas was subsequently introduced into the mass spectrometer and analyzed for its $^{15}N/^{14}N$ ratio. Reference gases were calibrated relative to standards IAEA–N1, –N2, and –N3 and in-house standards (B2151-high organic content sediment, B2153-low organic content soil, B2155-protein, B2157-wheat flour, and B2159-sorghum flour). Data were calibrated with USGS65 (Glycine) and USGS61 (Caffeine) and reported using delta notation relative to atmospheric N_2 in per mil ($\delta^{15}N_{org}$; ‰) with a standard precision of ±0.2‰.

4. Results

4.1. Geochemical proxies based on major and trace element geochemistry

Calcareous mudstones samples are mainly composed of SiO_2 (55.7%–68.7%), Al_2O_3 (14.9%–17.5%), CaO (1.1%–12.5%), MgO (2.3%–5.7%), K_2O (3.6%–8.7%), Na_2O (0.7%–2.0%), and Fe_2O_3 (4.8%–6.5%), with low content of P_2O_5 (<1.9%), TiO_2 (<0.9%), and MnO (<0.07%). Specifically, the wt% of most oxides fluctuate within narrow ranges between 9.1 and 14 m and 17.4 and 19.9 m (Table S1). The wt% of Na_2O, Fe_2O_3, MnO, and TiO_2 increase abruptly and then remains stable between 14 and 17.4 m (Table S1), which may be the result of increased sediment grain size (Jiang et al., 2023). The weathering proxies CIA, CIW, CIX and PIA exhibit similar trends, with a small decreasing trend between 9.1 and 12.2 m, a slight increasing trend between 12.2 and 14 m and relatively low yet stable values between 14

and 17.4 m (Fig. 6).

The utilization of trace element enrichment factors (X_{EF}) allows for the discernment of changes in terrigenous sediment provenance (*e.g.*, Ti_{EF}, Zr_{EF}, Sc_{EF}), primary productivity (*e.g.*, P_{EF}, Ba_{EF}, Ni_{EF}, Cu_{EF}) and redox conditions (*e.g.*, U_{EF}, V_{EF}) (Tribovillard et al., 2006). The Ti_{EF}, Zr_{EF}, and Sc_{EF} values are relatively stable (Fig. 4), with an average of 1.1, 1.2 and 1.0 respectively. Both Ti_{EF} and Zr_{EF} values display a small increase between 14 and 17.4 m, averaging 1.2 and 1.4 respectively. All mudstone samples uniformly exhibit a notably flat PAAS normalized REE distribution pattern (Fig. 4). The productivity-sensitive proxies (P_{EF}, Ba_{EF}, Ni_{EF} and Cu_{EF}) show two peaks within the 10.4–11.6 m and 12–13.2 m intervals, maintain relatively low values between 9.1 and 10.4 m, and exhibit small fluctuations within 13.2–19.9 m (Fig. 7). The trends of redox-sensitive proxies U_{EF} and V_{EF} closely follow those observed for the productivity-sensitive proxies (Fig. 7).

4.2. Magnetic susceptibility

Magnetic susceptibility (χ) values are generally low, ranging from 7.8 to 13.07 $\times 10^{-8}$ m^3 kg^{-1} (average = 9.95 $\times 10^{-8}$ m^3 kg^{-1}) (Fig. 2). The lower half of the section between 9.1 and 13.4 m is weakly magnetic (average = 9.64 $\times 10^{-8}$ m^3 kg^{-1}) and the upper half of the section between 13.4 and 19.75 m is more strongly magnetic (average = 10.12 $\times 10^{-8}$ m^3 kg^{-1}). Magnetic susceptibility is positively correlated with total wt% Fe_2O_3 ($R = 0.58$) and inversely correlated with wt% $CaCO_3$ ($R = 0.41$) and Al_2O_3/TiO_2 ($R = 0.38$) (Table S1). Weak positive correlations are also observed between χ and vanadium (V) (R = 0.38) and χ and barium (Ba) (R = 0.38) (Table S1). A small increase in χ values occurs over the interval 10.2–11.6 m, coincident with the negative carbon isotope excursion.

4.3. Nitrogen isotopes

The $\delta^{15}N_{org}$ values of mudstones range from 4.1 to 6.2‰ with an average of 5.3‰ (Fig. 2). Notably, the $\delta^{15}N_{org}$ values increase at 10.4 m and persists at relatively elevated levels until 13.6 m and fluctuates between 5.2 and 6.2‰ (average 5.6‰). In contrast, the $\delta^{15}N_{org}$ displays relatively low values spanning from 4.8 to 5.9‰ (average 5.3‰) within 9.1–10.4 m, and exhibit fluctuations between 4.1 and 5.8‰ (average 5.0‰) at 13.6–19.9 m (Fig. 2).

5. Discussion

5.1. Changes in sediment provenance and chemical weathering across the POE

Multiple geochemical proxies suggest that the sediment provenance within the study area remained largely unchanged across the POE. All mudstone samples plot into the continental island arc field of tectonic discrimination diagrams (Fig. 3), implying that the sediments were likely derived from an active tectonic setting (Bhatia and Crook, 1986). This is consistent with the active tectonic background characterized by initial uplift, northward indentation and north-verging thrusting of the Pamir during the Paleocene influenced by the India-Asia continental collision (Chen et al., 2018; Zhang et al., 2019). Key provenance proxies (Al_2O_3/TiO_2, Ti_{EF}, Zr_{EF}, Sc_{EF}, and ΣREE) display small variability, suggesting relatively constant source materials preceding the PETM. The Al_2O_3/TiO_2 ratio serves as a proxy for sediment provenance owing to the immobility of Al and Ti during sediment transport and weathering processes (Panahi et al., 2000; Young and Nesbitt, 1998). Moreover, Ti, Zr and Sc, all highly inert elements and often associated with heavy minerals, can offer valuable insights into shifts in sediment provenance, although their wt% can be affected by grain size variations (Scheffler et al., 2006; Yang et al., 2022; Zhou et al., 2015). For example, larger grain sizes are often associated with more abundant heavy minerals (McLennan et al., 1993). Additionally, the behavior of rare earth elements (REEs) in detrital sediment is primarily controlled by source rock attributes with minimal impact from sediment transport, weathering and diagenetic processes, making them sensitive indicators of sediment provenance (McLennan, 2018; Murray et al., 1990). Samples from pre-POE, POE, and post-POE intervals exhibit similar REE distribution patterns and ΣREE content, reinforcing the suggested stable sediment sources preceding the PETM (Fig. 4).

Most mudstone samples follow the ideal weathering path as shown in the A-CN-K diagram and CIX-WIP plot (Fig. 5), indicating negligible effects from potassium alteration and sediment reworking. This suggests that the chemical weathering signals of their source rocks are well preserved (Dinis et al., 2017; Fedo et al., 1995; Garzanti et al., 2013; Nesbitt and Young, 1984). Similar to provenance proxies, a coarsening in grain size would decrease weathering proxy values (*e.g.*, CIA, CIX, CIW, and PIA) due to the higher Na and Ca content and lower Al content of coarse-grained sediments relative to finer grained sediments (Fu et al., 2023; Lupker et al., 2013; Yang et al., 2020; Zhang et al., 2021). Consequently, chemical weathering proxies of the fine-grained samples are used to discuss the weathering trend, excluding those samples

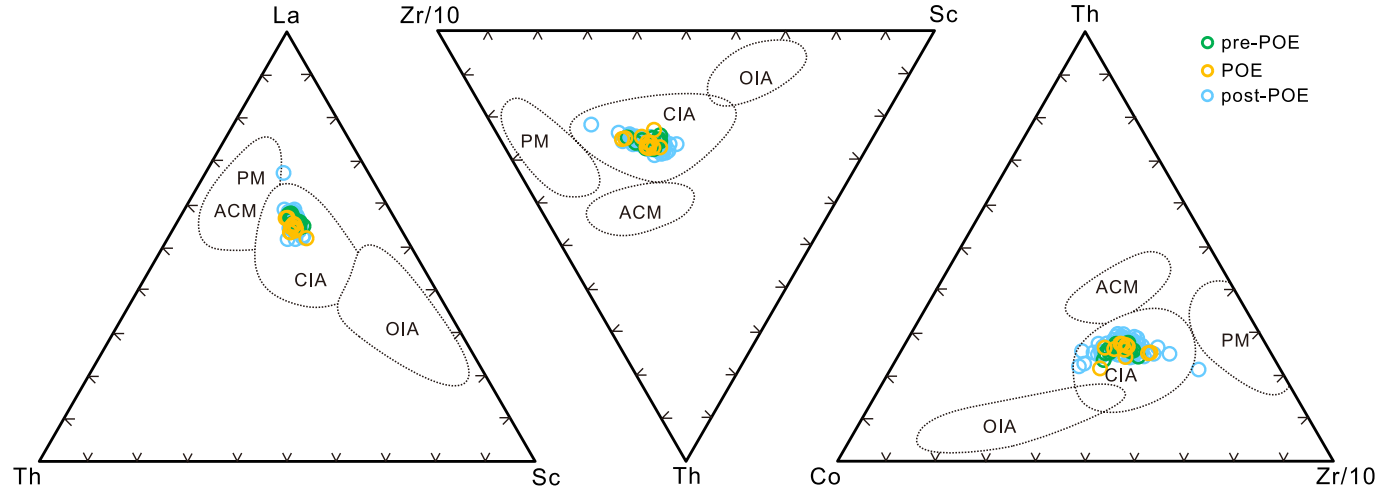

Fig. 3. Tectonic setting discrimination diagrams of mudstones, including La-Th-Sc, Th-Sc-Zr/10, Th-Co-Zr/10 ternary diagram (Bhatia and Crook, 1986); OIA: oceanic island arc; CIA: continental island arc; ACM: active continental margin; PM: passive margin.

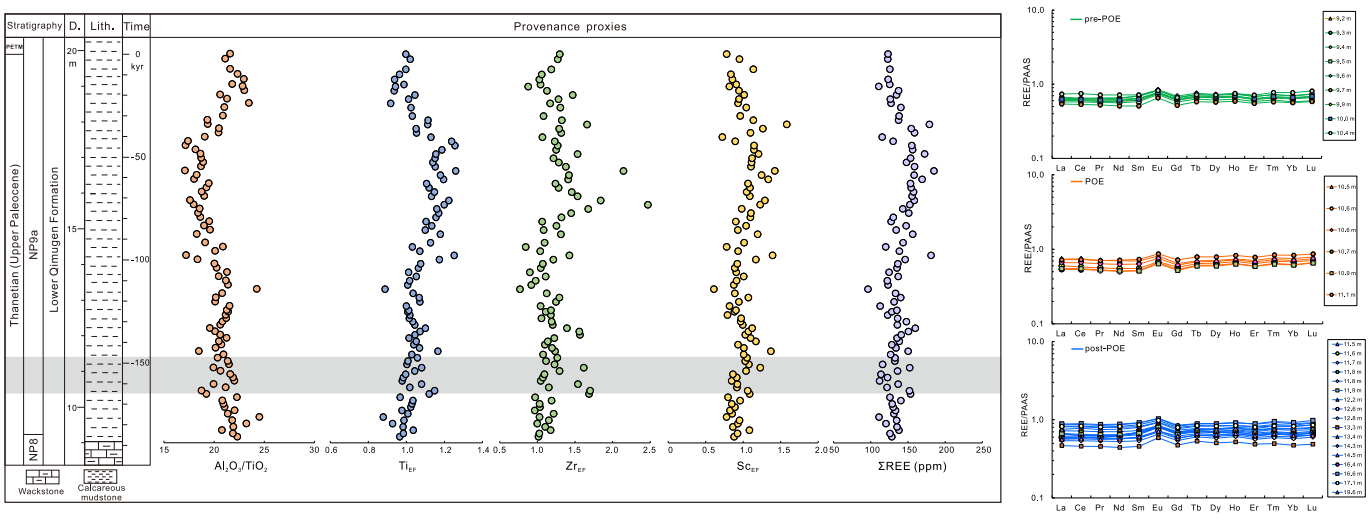

Fig. 4. Stratigraphic profiles of provenance proxies and REE patterns of mudstone samples. The provenance proxies include Al_2O_3/TiO_2 ratio, Ti_{EF}, Zr_{EF}, Sc_{EF} and ΣREE (EF = enrichment factor, Tribovillard et al., 2006). The gray shaded area shows the position of the POE (10.4–11.4 m). The REE patterns of pre-POE, POE, and post-POE samples are similar.

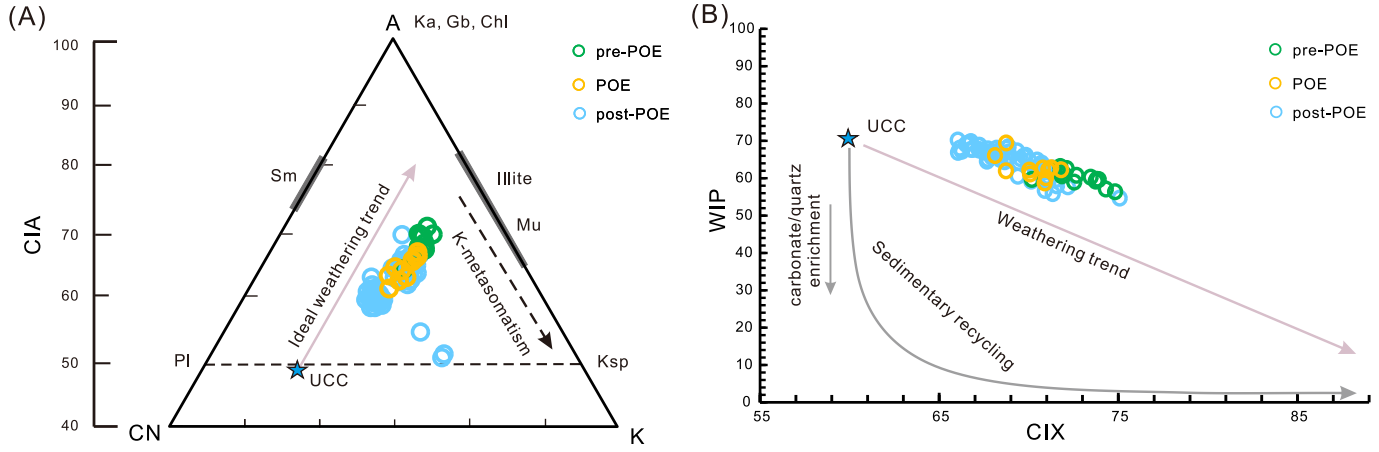

Fig. 5. (A) A-CN-K (Al_2O_3-CaO+Na_2O*-K_2O) diagram (Fedo et al., 1995) and (B) CIX-WIP plot (Dinis et al., 2017) for the analyzed mudstone samples. The UCC value (upper continental crust; star) is from Taylor and McLennan (1985). Pl: plagioclase; Ksp: K-feldspar; Sm: smectite; Mu: muscovite; Ka: kaolinite; Gb: gibbsite; Chl: chlorite.

associated with coarser grain size from 14 to 17.4 m. The increased values of several weathering proxies (CIA, CIX, CIW, and PIA) and a decrease in WIP indicate enhanced chemical weathering due to the loss of soluble elements like Ca, Na, and K from feldspars relative to refractory elements such as Al and Ti (Fedo et al., 1995; Nesbitt and Young, 1982). Additionally, the increase in the Rb/Sr ratio, a widely adopted weathering indicator, signifies intensified chemical weathering owing to the greater susceptibility to weathering of Sr-rich calcium-bearing minerals (*e.g.*, plagioclase, carbonate, and amphibole) compared to the relatively more resilient Rb-rich potassium-bearing minerals (*e.g.*, K-feldspar, biotite, and muscovite) (Chang et al., 2013; Jin et al., 2006; McLennan et al., 1993). All weathering proxies suggest stable chemical weathering conditions during the POE but increased chemical weathering following the POE (Fig. 6). This post-POE increase in chemical weathering is likely due to a delayed response to the higher atmospheric pCO_2 and temperature during the POE, because the response time of chemical weathering (*i.e.*, hundreds of thousands of years) is commonly longer than the suggested duration of the POE (*i.e.*, millennia to sub-millennia timescales) (Babila et al., 2022; Bowen et al., 2015; Colbourn et al., 2015; Walker and Kasting, 1992).

5.2. Marine nutrient and redox changes across the POE

Higher marine primary productivity in the shallow water of the eastern Tethys seaway during the POE and post-POE intervals is supported by the elevated values of productivity-sensitive proxies, including P_{EF}, Ba_{EF}, Cu_{EF}, and Ni_{EF} (Fig. 7). A comprehensive assessment of paleo-productivity based on multiple proxies is considered more reliable, given that no single indicator can accurately delineate changes in productivity due to influences from various factors such as redox conditions, sedimentation rates, mineral effects, or fluctuations in organic matter content (Averyt and Paytan, 2004; Schoepfer et al., 2015; Tribovillard, 2021). Phosphorus (P) is a critical nutrient for marine organisms, primarily entering shallow seas through continental weathering and riverine influx, exerting significant impact on marine primary productivity (Howarth, 1988; Paytan and McLaughlin, 2007; Tyrrell, 1999). Within the euphotic zone, biologically available P can be actively assimilated by phytoplankton, subsequently released in dissolved inorganic and organic forms, and ultimately accumulate in bottom sediments as settling particles (Paytan and McLaughlin, 2007). The shallow marine environment of the study area would have facilitated P mineralization within the water column and its subsequent preservation in the

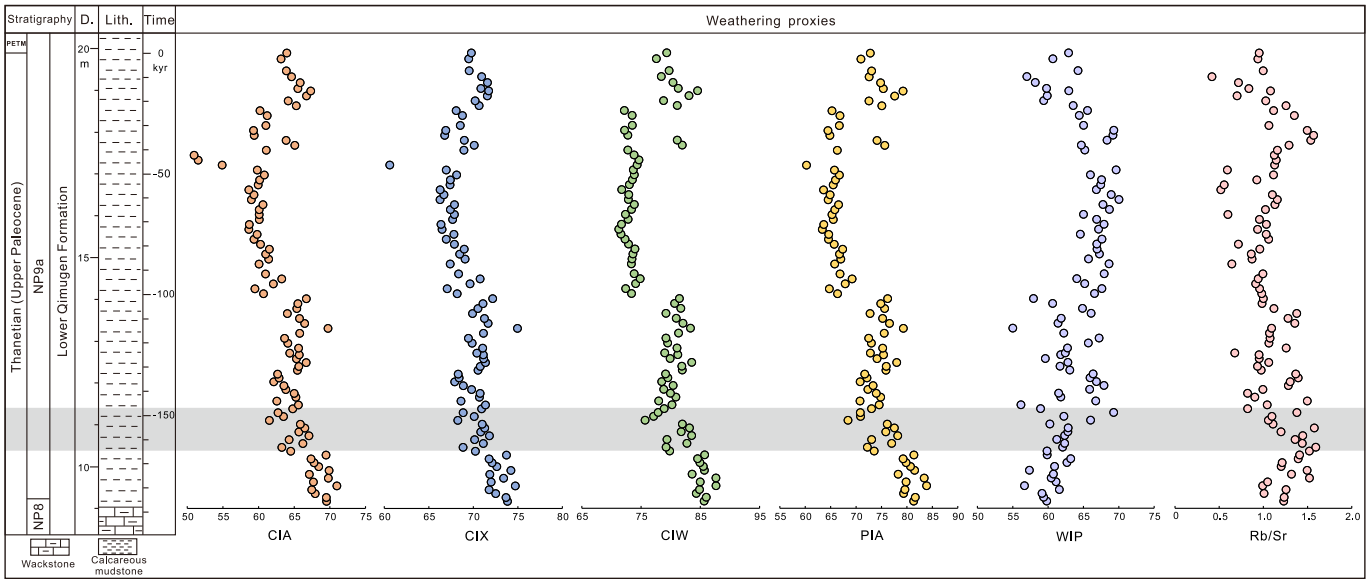

Fig. 6. Chemical weathering proxies based on CIA, CIX, CIW, PIA, WIP, and Rb/Sr across the POE. The gray shaded area shows the position of the POE (10.4–11.4 m). CIA: Chemical Index of Alteration; CIX: modified Chemical Index of Alteration; CIW: Chemical Index of Weathering; PIA: Plagioclase Index of Alteration; WIP: Weathering Index of Parker.

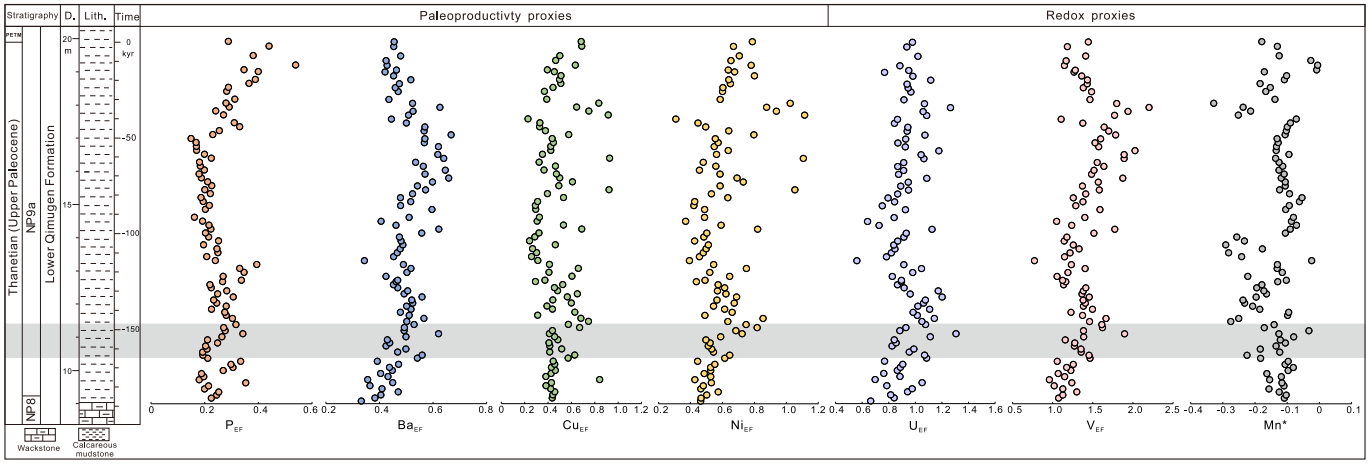

Fig. 7. Productivity proxies (P_{EF}, Ba_{EF}, Cu_{EF} and Ni_{EF}) and redox proxies (U_{EF}, V_{EF} and Mn*) across the POE. The gray shaded area shows the position of the POE (10.4–11.4 m). Mn* is calculated based on $Mn^* = \log[(Mn_{sample}/Mn_{shales})/(Fe_{sample}/Fe_{shales})]$), in which Mn_{shales} and Fe_{shales} are 600 and 46,150 ppm, respectively (Cullers, 2002; Wedepole et al., 1978). The subscript EF: enrichment factors (Tribovillard et al., 2006).

sediments (Algeo and Ingall, 2007; Ozaki et al., 2011; Watson, 2016). Similar to P, the primary source of Ba in seawater is from river input, while the Ba in marine sediments originates primarily from the burial of barite ($BaSO_4$) (Schoepfer et al., 2015). The formation of a substantial portion of barite correlates with organic matter decomposition (Horner et al., 2021; Paytan and Griffith, 2007; Schoepfer et al., 2015), and biofilms may facilitate the precipitation of $BaSO_4$ nanoparticles from seawater (Deng et al., 2019; Martinez-Ruiz et al., 2019). Therefore, increases in P_{EF} and Ba_{EF} likely indicate higher primary productivity in the eastern Tethys seaway. Additionally, Ni and Cu are also bioessential elements crucial for organisms and may concentrate within sediments *via* complexation with organic ligands in relatively oxygenated marine settings, thereby serving as indicators of primary productivity (Horner et al., 2021; Tribovillard et al., 2006). Therefore, synchronous increases in Ni_{EF} and Cu_{EF} further supports the inferred increase in primary productivity. During the POE, a rise in temperature may have resulted in increased precipitation and intensified river runoff, leading to an elevated nutrient influx into the ocean and consequently enhancing primary productivity (Peterson et al., 2000; Salles et al., 2023; Schoepfer et al., 2015). During the post-POE phase, terrestrial detritus and nutrients may have been transported into the ocean through enhanced continental weathering and river runoff, leading to higher primary productivity (Algeo and Scheckler, 1998; Dong et al., 2022; Shen et al., 2015; Wu et al., 2024).

The magnetic susceptibility (χ) in marine sediments can also track changes in terrigenous *vs.* biogenic sedimentation (Liu et al., 2013; Verosub and Roberts, 1995). The study area may have received sediments from rivers that eroded continental bedrocks, sediments, and soils due to its geographical location in the shallow eastern Tethys seaway that extended inland (Bosboom et al., 2011; Xi et al., 2016; Zhang et al., 2018). The magnetic properties of marine sediments are controlled by the iron oxide mineralogy, concentration of ferrimagnetic minerals relative to paramagnetic and diamagnetic minerals, and magnetic domain state of the ferrimagnetic minerals, which is in turn a function of grain volume (Liu et al., 2013; Verosub and Roberts, 1995). The low-field magnetic susceptibility of marine sediments is primarily

controlled by the concentrations of magnetite (Fe_3O_4). As carbonate productivity increased, χ values decreased due to dilution of terrigenous sediment with carbonate. A slight increase in χ values occurred concomitant with the POE, likely due to increased river runoff and transfer of terrigenous Fe-Ti oxides into the Tethys seaway. This may be attributed to the intensification of precipitation and river runoff resulting from elevated temperatures during the POE. A second increase in χ is observed at 13.4 m, coinciding with a decrease in $CaCO_3$ productivity in the post-POE interval.

Elevated productivity may have led to a subsequent moderate decline in dissolved oxygen in the shallow marine environment, which is evidenced by increased V_{EF} and U_{EF} values and a decrease in Mn* values (Fig. 7). Under reducing conditions, soluble hexavalent uranium (U) can transform into insoluble tetravalent U and accumulate within sediments (Algeo and Maynard, 2004; Tribovillard et al., 2006). V exhibits a shift from soluble pentavalent V to insoluble tetravalent V under mild reducing conditions (*e.g.*, suboxic), while more extreme reducing conditions (*e.g.*, euxinia) can further facilitate its conversion into insoluble trivalent V (Tribovillard et al., 2006; Wanty and Goldhaber, 1992). Thus, the slight increase in U_{EF} and V_{EF} after the onset of POE at the study site suggests a moderate deoxygenation within the shallow ocean. Additionally, the slight decrease noted in the Mn* value also implies a moderate increase in the reduction state of the bottom water. This is because the prevalence of iron precipitation as sulfides occurs prominently under severe reducing conditions, whereas Mn tends to accumulate under more oxygenated conditions and forms soluble cations under relatively less reducing states (Cullers, 2002; Takahashi et al., 2014). Therefore, the slightly elevated V_{EF} and U_{EF} values along with the decreased Mn* values suggest a mild bottom-water deoxygenation during the POE.

The $\delta^{15}N_{org}$ of marine sediments can be used as an indicator of ancient ocean productivity and redox conditions (Algeo et al., 2014; Casciotti, 2016; Galbraith et al., 2004; Stüeken et al., 2016). Preceding the POE, $\delta^{15}N_{org}$ values are relatively high (averaging 5.4‰), but lower than the $\delta^{15}N$ measured from foraminifera shell-bound organic matter (~8–10 ‰ *v*) observed in global oceans (including the North Pacific, North Atlantic, and South Atlantic) during the Late Paleocene, suggesting increased denitrification rates in the water column (Junium et al., 2018; Kast et al., 2019). During the POE and its immediate aftermath, $\delta^{15}N_{org}$ values increased, indicating a slight expansion of Oxygen Minimum Zones (OMZs) in the open sea that led to enhanced denitrification under more suboxic or anoxic conditions (Algeo et al., 2014; Kast et al., 2019; Liu et al., 2008). Denitrification in the water column, a process involving the biological reduction of nitrate (NO_3^-) to N_2 in oxygen-depleted environments, contributes to ^{15}N enrichment within the remaining NO_3^- reservoir in seawater, which is utilized by marine organisms and subsequently preserved in sediments (Capone et al., 2008). The expansion of OMZs within the open sea is associated with elevated atmospheric CO_2 levels during the POE, driving nutrient-rich riverine inputs into the marine ecosystem, thereby promoting primary productivity and exacerbating deoxygenation. A slight decrease in $\delta^{15}N_{org}$ following the POE may be attributed to the contraction of the OMZs resulting from reduced primary productivity. Alternatively, continual denitrification processes may have contributed to the sustained depletion of the NO_3^- reservoir, which in turn prompted more ^{15}N-depleted nitrogen uptake from the atmosphere through biological N_2 fixation (Bauersachs et al., 2009; Capone et al., 2008; Liu et al., 2020).

5.3. Implications of global POE records

The POE is a global warming event that occurred prior to the PETM, but with a smaller temperature rise than the PETM (Babila et al., 2022; Doubrawa et al., 2022). Compared to the PETM, which has been documented in marine and terrestrial sediments worldwide (Cui et al., 2021; Koch et al., 1992; McInerney and Wing, 2011; Nunes and Norris, 2006; Vimpere et al., 2023; Westerhold et al., 2018), the POE has only been reported in shallow marine and terrestrial settings, but not in deep-sea sedimentary records. This likely results from the short duration of the event, relatively small amount of carbon emissions, and potential processes such as sediment mixing, carbonate dissolution, and bioturbation in the deep-sea environment (Babila et al., 2022; Bard, 2001). The POE has been identified in shallow marine settings, such as the Maryland and New Jersey Coastal Plains in the United States (Babila et al., 2022; Doubrawa et al., 2022; Sluijs et al., 2007), the North Sea Basin (Kender et al., 2012), the Pyrenean foreland basins (Tremblin et al., 2022), and the Tasman Sea (Elling et al., 2019), as well as the terrestrial Bighorn Basin in Wyoming, western United States (Bowen et al., 2015) (Fig. 1A). The similar trends of $\delta^{13}C$ records across diverse marine and continental settings underscore the global significance of the POE event (Babila et al., 2022). Although the temperature increase was small (~ 2 to 5 °C) during the POE, nutrient input may have been enhanced *via* intensified precipitation and river runoff, promoting marine primary productivity and consequent deoxygenation in the shallow seaways of the eastern Tethys. Similarly, the enrichment of large amount of authigenic glauconites in sediments depoited in shelf settings of the southern Tethys was also attributed to intensified continental weathering, riverine runoff and oxygen-depleted conditions (Banerjee et al., 2020; Choudhury et al., 2021). Although the POE was not well expressed in the deep sea, there may still be corresponding environmental effects attributable to the carbon emissions during the POE. For example, in the Northwest Atlantic, deep-sea deoxygenation intensified several hundred thousand years before the PETM, peaking approximately 50 kyr before the PETM, potentially associated with the POE despite the lack of direct documentation (Xue et al., 2023). Therefore, while the POE has thus far only been reported from high-resolution shallow marine and terrestrial records, its associated environmental responses—including amplified continental weathering, ocean deoxygenation, and ocean acidification—may hold broader implications that warrant further investigation.

6. Conclusions

We conducted a comprehensive paleoenvironmental reconstruction of the eastern Tethys during the POE using high-resolution geochemical and magnetic susceptibility records from the shallow marine Kuzigongsu section in the Tarim Basin, China. The POE can provide an ancient analogue for rapid climatic and environmental changes caused by anthropogenic CO_2 emissions.

Small fluctuations in heavy mineral-associated inert elements (Ti, Zr, and Sc) and highly similar REE distribution patterns before, during, and after the POE suggest stable sediment provenance. This aligns with an increase in χ values across the POE, with χ values primarily controlled by terrigenous sediment supply and variable dilution with $CaCO_3$. Enhanced chemical weathering during the post-POE phase is inferred from chemical weathering proxies (*e.g.*, CIA, CIW, CIX, and PIA) and Rb/Sr ratio.

Increased marine primary productivity driven by elevated pCO_2 and temperature led to mild oceanic deoxygenation during the POE, which is corroborated by productivity-sensitive proxies (P_{EF}, Ba_{EF}, Ni_{EF}, and Cu_{EF}) and redox-sensitive proxies (U_{EF} and V_{EF}). The increased $\delta^{15}N_{org}$ values suggest enhanced denitrification during the POE, further confirming intensified reducing conditions of the eastern Tethys.

CRediT authorship contribution statement

Yixin Dong: Writing – review & editing, Writing – original draft, Visualization, Formal analysis, Funding acquisition, Investigation, Methodology. **Anthony Gachetti:** Investigation, Methodology, Writing – review & editing. **Qingting Wu:** Formal analysis, Methodology, Writing – review & editing. **Maurizia De Palma:** Investigation, Methodology, Writing – review & editing. **Xiumian Hu:** Investigation,

Writing – review & editing. **Stefanie Brachfeld:** Investigation, Methodology, Writing – review & editing. **Zhilin Yang:** Investigation, Writing – review & editing. **Jiuyuan Wang:** Investigation, Methodology, Writing – review & editing. **Yasu Wang:** Formal analysis, Writing – review & editing. **Shijun Jiang:** Writing – review & editing, Methodology, Investigation, Funding acquisition, Conceptualization. **Ying Cui:** Writing – review & editing, Visualization, Validation, Supervision, Resources, Project administration, Methodology, Investigation, Funding acquisition, Formal analysis, Conceptualization.

Declaration of competing interest

The authors declare no competing interests.

Data availability

Supplementary data are provided in supplementary table.

Acknowledgments

We thank Dr. Xiaona Li for assisting with ICP-MS and stable nitrogen isotope analysis. This study was supported by the National Key Research and Development Program of China (2022YFF0800800), the National Natural Science Foundation of China (41888101), and Southern Marine Science and Engineering Guangdong Laboratory (Zhuhai) (No. SML2023SP206) to S.J. Y.C. is supported by the National Science Foundation (2002370, 2026877). Y.D. is supported by the Natural Science Foundation of Sichuan Province (No. 2023NSFSC0804). National Science Foundation grants EAR-1839313 and PP-1342000 co-funded Montclair's Kappabridge. This is a contribution to the UNESCO IGCP 739.

Appendix A. Supplementary data

Supplementary data to this article can be found online at https://doi.org/10.1016/j.palaeo.2024.112234.

References

Algeo, T.J., Ingall, E., 2007. Sedimentary Corg: P ratios, paleocean ventilation, and Phanerozoic atmospheric pO_2. Palaeogeogr. Palaeoclimatol. Palaeoecol. 256, 130–155.
Algeo, T.J., Maynard, J.B., 2004. Trace-element behavior and redox facies in core shales of Upper Pennsylvanian Kansas-type cyclothems. Chem. Geol. 206, 289–318.
Algeo, T.J., Scheckler, S.E., 1998. Terrestrial-marine teleconnections in the Devonian: links between the evolution of land plants, weathering processes, and marine anoxic events. Philos. Trans. R. Soc. Lond. B Biol. Sci. 353, 113–130.
Algeo, T.J., Meyers, P.A., Robinson, R.S., Rowe, H., Jiang, G.Q., 2014. Icehouse–greenhouse variations in marine denitrification. Biogeosciences 11, 1273–1295.
Averyt, K.B., Paytan, A., 2004. A comparison of multiple proxies for export production in the equatorial Pacific. Paleoceanography 19.
Aziz, H.A., Hilgen, F.J., van Luijk, G.M., Sluijs, A., Kraus, M.J., Pares, J.M., Gingerich, P. D., 2008. Astronomical climate control on paleosol stacking patterns in the upper Paleocene–lower Eocene Willwood Formation, Bighorn Basin, Wyoming. Geology 36, 531–534.
Babila, T.L., Rosenthal, Y., Wright, J.D., Miller, K.G., 2016. A continental shelf perspective of ocean acidification and temperature evolution during the Paleocene-Eocene thermal Maximum. Geology 44, 275–278.
Babila, T.L., Penman, D.E., Standish, C.D., Doubrawa, M., Bralower, T.J., Robinson, M. M., Self-Trail, J.M., Speijer, R.P., Stassen, P., Foster, G.L., 2022. Surface ocean warming and acidification driven by rapid carbon release precedes Paleocene-Eocene Thermal Maximum. Sci. Adv. 8, eabg1025.
Banerjee, S., Choudhury, T.R., Saraswati, P.K., Khanolkar, S., 2020. The formation of authigenic deposits during Paleogene warm climatic intervals: a review. J. Palaeogeogr. 9, 1–27.
Bard, E., 2001. Paleoceanographic implications of the difference in deep-sea sediment mixing between large and fine particles. Paleoceanography 16, 235–239.
Bauersachs, T., Schouten, S., Compaoré, J., Wollenzien, U., Stal, L.J., Sinninghe Damsteé, J.S., 2009. Nitrogen isotopic fractionation associated with growth on dinitrogen gas and nitrate by cyanobacteria. Limnol. Oceanogr. 54, 1403–1411.
Bhatia, M.R., Crook, K.A.W., 1986. Trace element characteristics of graywackes and tectonic setting discrimination of sedimentary basins. Contrib. Mineral. Petrol. 92, 181–193.
Bosboom, R.E., Dupont-Nivet, G., Houben, A.J.P., Brinkhuis, H., Villa, G., Mandic, O., Stoica, M., Zachariasse, W.J., Guo, Z., Li, C., 2011. Late Eocene sea retreat from the Tarim Basin (west China) and concomitant Asian paleoenvironmental change. Palaeogeogr. Palaeoclimatol. Palaeoecol. 299, 385–398.
Bowen, G.J., Maibauer, B.J., Kraus, M.J., Röhl, U., Westerhold, T., Steimke, A., Gingerich, P.D., Wing, S.L., Clyde, W.C., 2015. Two massive, rapid releases of carbon during the onset of the Palaeocene–Eocene thermal maximum. Nat. Geosci. 8, 44–47.
Cao, W., Xi, D., Melinte-Dobrinescu, M.C., Jiang, T., Wise Jr., S.W., Wan, X., 2018. Calcareous nannofossil changes linked to climate deterioration during the Paleocene–Eocene thermal maximum in Tarim Basin, NW China. Geosci. Front. 9, 1465–1478.
Capone, D.G., Bronk, D.A., Mulholland, M.R., Carpenter, E.J., 2008. Nitrogen in the Marine Environment. Elsevier.
Carmichael, M.J., Pancost, R.D., Lunt, D.J., 2018. Changes in the occurrence of extreme precipitation events at the Paleocene–Eocene thermal maximum. Earth Planet. Sci. Lett. 501, 24–36.
Casciotti, K.L., 2016. Nitrogen and oxygen isotopic studies of the marine nitrogen cycle. Annu. Rev. Mar. Sci. 8, 379–407.
Chang, H., An, Z., Wu, F., Jin, Z., Liu, W., Song, Y., 2013. A Rb/Sr record of the weathering response to environmental changes in westerly winds across the Tarim Basin in the late Miocene to the early Pleistocene. Palaeogeogr. Palaeoclimatol. Palaeoecol. 386, 364–373.
Chen, X., Chen, H., Lin, X., Cheng, X., Yang, R., Ding, W., Gong, J., Wu, L., Zhang, F., Chen, S., 2018. Arcuate Pamir in the Paleogene? Insights from a review of stratigraphy and sedimentology of the basin fills in the foreland of NE Chinese Pamir, western Tarim Basin. Earth Sci. Rev. 180, 1–16.
Chen, Z., Ding, Z., Yang, S., Sun, J., Zhu, M., Xiao, Y., Tong, F., Liang, Y., 2023. Strong coupling between carbon cycle, climate, and weathering during the paleocene-eocene thermal maximum. Geophys. Res. Lett. 50 e2023GL102897.
Choudhury, T.R., Banerjee, S., Khanolkar, S., Saraswati, P.K., Meena, S.S., 2021. Glauconite authigenesis during the onset of the Paleocene-Eocene thermal Maximum: a case study from the Khuiala Formation in Jaisalmer Basin, India. Palaeogeogr. Palaeoclimatol. Palaeoecol. 571, 110388.
Clarkson, M.O., Lenton, T.M., Andersen, M.B., Bagard, M.-L., Dickson, A.J., Vance, D., 2021. Upper limits on the extent of seafloor anoxia during the PETM from uranium isotopes. Nat. Commun. 12, 399.
Colbourn, G., Ridgwell, A., Lenton, T.M., 2015. The time scale of the silicate weathering negative feedback on atmospheric CO_2. Glob. Biogeochem. Cycles 29, 583–596.
Cui, Y., Diefendorf, A.F., Kump, L.R., Jiang, S., Freeman, K.H., 2021. Synchronous marine and terrestrial carbon cycle perturbation in the high arctic during the PETM. Paleoceanogr. Paleoclimatol. 36 e2020PA003942.
Cullers, R.L., 2002. Implications of elemental concentrations for provenance, redox conditions, and metamorphic studies of shales and limestones near Pueblo, CO, USA. Chem. Geol. 191, 305–327.
Deng, N., Stack, A.G., Weber, J., Cao, B., De Yoreo, J.J., Hu, Y., 2019. Organic–mineral interfacial chemistry drives heterogeneous nucleation of Sr-rich $(Ba_x, Sr_{1-x})\ SO_4$ from undersaturated solution. Proc. Natl. Acad. Sci. 116, 13221–13226.
Dinis, P., Garzanti, E., Vermeesch, P., Huvi, J., 2017. Climatic zonation and weathering control on sediment composition (Angola). Chem. Geol. 467, 110–121.
Dong, Y., Convers, L.C., Jiang, S., Li, X., Zhu, P., Chen, H., Cui, Y., 2022. Reconstruction of the early Eocene paleoclimate and paleoenvironment of the southeastern Neo-Tethys Ocean. Glob. Planet. Chang. 215, 103875.
Doubrawa, M., Stassen, P., Robinson, M.M., Babila, T.L., Zachos, J.C., Speijer, R.P., 2022. Shelf Ecosystems along the US Atlantic Coastal Plain prior to and during the Paleocene-Eocene thermal Maximum: Insights into the Stratigraphic Architecture. Paleoceanogr. Paleoclimatol. 37 e2022PA004475.
Elling, F.J., Gottschalk, J., Doeana, K.D., Kusch, S., Hurley, S.J., Pearson, A., 2019. Archaeal lipid biomarker constraints on the Paleocene-Eocene carbon isotope excursion. Nat. Commun. 10, 4519.
Fedo, C.M., Wayne Nesbitt, H., Young, G.M., 1995. Unraveling the effects of potassium metasomatism in sedimentary rocks and paleosols, with implications for paleoweathering conditions and provenance. Geology 23, 921–924.
Frieling, J., Gebhardt, H., Huber, M., Adekeye, O.A., Akande, S.O., Reichart, G.-J., Middelburg, J.J., Schouten, S., Sluijs, A., 2017. Extreme warmth and heat-stressed plankton in the tropics during the Paleocene-Eocene thermal Maximum. Sci. Adv. 3, e1600891.
Fu, H., Jian, X., Pan, H., 2023. Bias in sediment chemical weathering intensity evaluation: a numerical simulation study. Earth Sci. Rev. 104574.
Galbraith, E.D., Kienast, M., Pedersen, T.F., Calvert, S.E., 2004. Glacial-interglacial modulation of the marine nitrogen cycle by high-latitude O_2 supply to the global thermocline. Paleoceanography 19.
Garzanti, E., Padoan, M., Setti, M., Najman, Y., Peruta, L., Villa, I.M., 2013. Weathering geochemistry and Sr-Nd fingerprints of equatorial upper Nile and Congo muds. Geochem. Geophys. Geosyst. 14, 292–316.
Garzanti, E., Padoan, M., Setti, M., López-Galindo, A., Villa, I.M., 2014. Provenance versus weathering control on the composition of tropical river mud (southern Africa). Chem. Geol. 366, 61–74.
Harnois, L., 1988. The CIW index: a new chemical index of weathering. Sediment. Geol. 55, 319–322.
Horner, T.J., Little, S.H., Conway, T.M., Farmer, J.R., Hertzberg, J.E., Janssen, D.J., Lough, A.J.M., McKay, J.L., Tessin, A., Galer, S.J.G., 2021. Bioactive trace metals and their isotopes as paleoproductivity proxies: An assessment using GEOTRACES-era data. Glob. Biogeochem. Cycles 35, e2020GB006814.
Howarth, R.W., 1988. Nutrient limitation of net primary production in marine ecosystems. Annu. Rev. Ecol. Syst. 19, 89–110.

Jiang, J., Hu, X., Li, J., Garzanti, E., Jiang, S., Cui, Y., Wang, Y., 2023. Eustatic change across the Paleocene-Eocene thermal Maximum in the epicontinental Tarim seaway. Glob. Planet. Chang. 229, 104241.
Jin, Z., Cao, J., Wu, J., Wang, S., 2006. A Rb/Sr record of catchment weathering response to Holocene climate change in Inner Mongolia. Earth Surf. Process. Landforms J. Br. Geomorphol. Res. Group 31, 285–291.
Jones, S.M., Hoggett, M., Greene, S.E., Jones, T.D., 2019. Large Igneous Province thermogenic greenhouse gas flux could have initiated Paleocene-Eocene thermal Maximum climate change. Nat. Commun. 10, 1–16.
Junium, C.K., Dickson, A.J., Uveges, B.T., 2018. Perturbation to the nitrogen cycle during rapid early Eocene global warming. Nat. Commun. 9, 3186.
Kast, E.R., Stolper, D.A., Auderset, A., Higgins, J.A., Ren, H., Wang, X.T., Martínez-García, A., Haug, G.H., Sigman, D.M., 2019. Nitrogen isotope evidence for expanded ocean suboxia in the early Cenozoic. Science 364, 386–389.
Kaya, M.Y., Dupont-Nivet, G., Proust, J.N., Roperch, P., Bougeois, L., Meijer, N., Frieling, J., Fioroni, C., Altıner, S.Ö., Vardar, E., 2019. Paleogene evolution and demise of the proto-Paratethys Sea in Central Asia (Tarim and Tajik basins): Role of intensified tectonic activity at ca. 41 Ma. Basin Res. 31, 461–486.
Kender, S., Stephenson, M.H., Riding, J.B., Leng, M.J., Knox, R.W.B., Peck, V.L., Kendrick, C.P., Ellis, M.A., Vane, C.H., Jamieson, R., 2012. Marine and terrestrial environmental changes in NW Europe preceding carbon release at the Paleocene–Eocene transition. Earth Planet. Sci. Lett. 353, 108–120.
Kiehl, J.T., Zarzycki, C.M., Shields, C.A., Rothstein, M.V., 2021. Simulated changes to tropical cyclones across the Paleocene-Eocene thermal Maximum (PETM) boundary. Palaeogeogr. Palaeoclimatol. Palaeoecol. 572, 110421.
Koch, P.L., Zachos, J.C., Gingerich, P.D., 1992. Correlation between isotope records in marine and continental carbon reservoirs near the Palaeocene/Eocene boundary. Nature 358, 319–322.
Li, W., Hu, X., Melinte-Dobrinescu, M.C., Boudagher-Fadel, M.K., Li, J., Zhang, S., Xu, Y., 2021. Early Paleogene hyperthermal events and their environmental impacts in the Qimugen section, Tarim Sea. Chin. Sci. Bull. 66, 1067–1082.
Liu, Z., Altabet, M.A., Herbert, T.D., 2008. Plio-Pleistocene denitrification in the eastern tropical North Pacific: Intensification at 2.1 Ma. Geochem. Geophys. Geosyst. 9.
Liu, Z., Liu, Q., Torrent, J., Barrón, V., Hu, P., 2013. Testing the magnetic proxy χFD/HIRM for quantifying paleoprecipitation in modern soil profiles from Shaanxi Province, China. Glob. Planet. Chang. 110, 368–378.
Liu, Y., Magnall, J.M., Gleeson, S.A., Bowyer, F., Poulton, S.W., Zhang, J., 2020. Spatio-temporal evolution of ocean redox and nitrogen cycling in the early Cambrian Yangtze Ocean. Chem. Geol. 554, 119803.
Lupker, M., France-Lanord, C., Galy, V., Lavé, J., Kudrass, H., 2013. Increasing chemical weathering in the Himalayan system since the last Glacial Maximum. Earth Planet. Sci. Lett. 365, 243–252.
Martinez-Ruiz, F., Paytan, A., Gonzalez-Muñoz, M.T., Jroundi, F., Abad, M.D.M., Lam, P. J., Bishop, J.K.B., Horner, T.J., Morton, P.L., Kastner, M., 2019. Barite formation in the ocean: Origin of amorphous and crystalline precipitates. Chem. Geol. 511, 441–451.
McInerney, F.A., Wing, S.L., 2011. The Paleocene-Eocene thermal Maximum: a perturbation of carbon cycle, climate, and biosphere with implications for the future. Annu. Rev. Earth Planet. Sci. 39, 489–516.
McLennan, S.M., 1993. Weathering and global denudation. J. Geol. 101, 295–303.
McLennan, S.M., 2018. Rare earth elements in sedimentary rocks; influence of provenance and sedimentary processes. Geochem. and Min. of Rare Earth Elements, 169–200.
McLennan, S.M., Hemming, S., McDaniel, D.K., Hanson, G.N., 1993. Geochemical approaches to sedimentation, provenance, and tectonics. Spec. Pap. Geol. Soc. America 21.
Murray, R.W., Buchholtz ten Brink, M.R., Jones, D.L., Gerlach, D.C., Russ Iii, G.P., 1990. Rare earth elements as indicators of different marine depositional environments in chert and shale. Geology 18, 268–271.
Nesbitt, H.W., Young, G.M., 1982. Early Proterozoic climates and plate motions inferred from major element chemistry of lutites. Nature 299, 715–717.
Nesbitt, H.W., Young, G.M., 1984. Prediction of some weathering trends of plutonic and volcanic rocks based on thermodynamic and kinetic considerations. Geochim. Cosmochim. Acta 48, 1523–1534.
Nunes, F., Norris, R.D., 2006. Abrupt reversal in ocean overturning during the Palaeocene/Eocene warm period. Nature 439, 60–63.
Ozaki, K., Tajima, S., Tajika, E., 2011. Conditions required for oceanic anoxia/euxinia: Constraints from a one-dimensional ocean biogeochemical cycle model. Earth Planet. Sci. Lett. 304, 270–279.
Panahi, A., Young, G.M., Rainbird, R.H., 2000. Behavior of major and trace elements (including REE) during Paleoproterozoic pedogenesis and diagenetic alteration of an Archean granite near Ville Marie, Québec, Canada. Geochim. Cosmochim. Acta 64, 2199–2220.
Paytan, A., Griffith, E.M., 2007. Marine barite: Recorder of variations in ocean export productivity. Deep-Sea Res. II Top. Stud. Oceanogr. 54, 687–705.
Paytan, A., McLaughlin, K., 2007. The oceanic phosphorus cycle. Chem. Rev. 107, 563–576.
Penman, D.E., Hönisch, B., Zeebe, R.E., Thomas, E., Zachos, J.C., 2014. Rapid and sustained surface ocean acidification during the Paleocene-Eocene thermal Maximum. Paleoceanography 29, 357–369.
Peterson, L.C., Haug, G.H., Hughen, K.A., Rohl, U., 2000. Rapid changes in the hydrologic cycle of the tropical Atlantic during the last glacial. Science 290, 1947–1951.
Pourmand, A., Dauphas, N., Ireland, T.J., 2012. A novel extraction chromatography and MC-ICP-MS technique for rapid analysis of REE, Sc and Y: revising CI-chondrite and Post-Archean Australian Shale (PAAS) abundances. Chem. Geol. 291, 38–54.
Rush, W.D., Kiehl, J.T., Shields, C.A., Zachos, J.C., 2021. Increased frequency of extreme precipitation events in the North Atlantic during the PETM: Observations and theory. Palaeogeogr. Palaeoclimatol. Palaeoecol. 568, 110289.
Salles, T., Husson, L., Lorcery, M., Hadler Boggiani, B., 2023. Landscape dynamics and the Phanerozoic diversification of the biosphere. Nature 624, 115–121.
Scheffler, K., Buehmann, D., Schwark, L., 2006. Analysis of late Palaeozoic glacial to postglacial sedimentary successions in South Africa by geochemical proxies–Response to climate evolution and sedimentary environment. Palaeogeogr. Palaeoclimatol. Palaeoecol. 240, 184–203.
Schoepfer, S.D., Shen, J., Wei, H., Tyson, R.V., Ingall, E., Algeo, T.J., 2015. Total organic carbon, organic phosphorus, and biogenic barium fluxes as proxies for paleomarine productivity. Earth Sci. Rev. 149, 23–52.
Shen, J., Schoepfer, S.D., Feng, Q., Zhou, L., Yu, J., Song, H., Wei, H., Algeo, T.J., 2015. Marine productivity changes during the end-Permian crisis and early Triassic recovery. Earth Sci. Rev. 149, 136–162.
Sluijs, A., Brinkhuis, H., Schouten, S., Bohaty, S.M., John, C.M., Zachos, J.C., Reichart, G.-J., Sinninghe Damsté, J.S., Crouch, E.M., Dickens, G.R., 2007. Environmental precursors to rapid light carbon injection at the Palaeocene/Eocene boundary. Nature 450, 1218–1221.
Sluijs, A., Van Roij, L., Harrington, G.J., Schouten, S., Sessa, J.A., LeVay, L.J., Reichart, G.J., Slomp, C.P., 2014. Warming, euxinia and sea level rise during the Paleocene–Eocene Thermal Maximum on the Gulf Coastal Plain: implications for ocean oxygenation and nutrient cycling. Clim. Past 10, 1421–1439.
Stokke, E.W., Jones, M.T., Tierney, J.E., Svensen, H.H., Whiteside, J.H., 2020. Temperature changes across the Paleocene-Eocene thermal Maximum–a new high-resolution TEX_{86} temperature record from the Eastern North Sea Basin. Earth Planet. Sci. Lett. 544, 116388.
Stramma, L., Johnson, G.C., Sprintall, J., Mohrholz, V., 2008. Expanding oxygen-minimum zones in the tropical oceans. Science 320, 655–658.
Stüeken, E.E., Kipp, M.A., Koehler, M.C., Buick, R., 2016. The evolution of Earth's biogeochemical nitrogen cycle. Earth Sci. Rev. 160, 220–239.
Takahashi, S., Yamasaki, S.-I., Ogawa, Y., Kimura, K., Kaiho, K., Yoshida, T., Tsuchiya, N., 2014. Bioessential element-depleted ocean following the euxinic maximum of the end-Permian mass extinction. Earth Planet. Sci. Lett. 393, 94–104.
Taylor, S.R., McLennan, S.M., 1985. The continental crust: its composition and evolution: an examination of the geochemical record preserved in sedimentary rocks. Blackwell Scientific, Oxford.
Tremblin, M., Khozyem, H., Adatte, T., Spangenberg, J.E., Fillon, C., Grauls, A., Hunger, T., Nowak, A., Läuchli, C., Lasseur, E., 2022. Mercury enrichments of the Pyrenean foreland basins sediments support enhanced volcanism during the Paleocene-Eocene thermal maximum (PETM). Glob. Planet. Chang. 212, 103794.
Tribovillard, N., 2021. Re-assessing copper and nickel enrichments as paleo-productivity proxies. Bulletin de la Société Géologique de France 192.
Tribovillard, N., Algeo, T.J., Lyons, T., Riboulleau, A., 2006. Trace metals as paleoredox and paleoproductivity proxies: an update. Chem. Geol. 232, 12–32.
Tyrrell, T., 1999. The relative influences of nitrogen and phosphorus on oceanic primary production. Nature 400, 525–531.
Verosub, K.L., Roberts, A.P., 1995. Environmental magnetism: past, present, and future. J. Geophys. Res. Solid Earth 100, 2175–2192.
Vimpere, L., Spangenberg, J.E., Roige, M., Adatte, T., De Kaenel, E., Fildani, A., Clark, J., Sahoo, S., Bowman, A., Sternai, P., 2023. Carbon isotope and biostratigraphic evidence for an expanded Paleocene–Eocene Thermal Maximum sedimentary record in the deep Gulf of Mexico. Geology 51, 334–339.
Walker, J.C.G., Kasting, J.F., 1992. Effects of fuel and forest conservation on future levels of atmospheric carbon dioxide. Glob. Planet. Chang. 5, 151–189.
Wang, Y., Cui, Y., Su, H., Jiang, J., Wang, Y., Yang, Z., Hu, X., Jiang, S., 2022. Response of calcareous nannoplankton to the Paleocene–Eocene Thermal Maximum in the Paratethys Seaway (Tarim Basin, West China). Glob. Planet. Chang. 217, 103918.
Wanty, R.B., Goldhaber, M.B., 1992. Thermodynamics and kinetics of reactions involving vanadium in natural systems: Accumulation of vanadium in sedimentary rocks. Geochim. Cosmochim. Acta 56, 1471–1483.
Watson, A.J., 2016. Oceans on the edge of anoxia. Science 354, 1529–1530.
Wedepohl, KH., 1978. Manganese: abundance in common sediments and sedimentary rocks. Handbook of Geochemistry, 2. Springer, Berlin, pp. 1–17.
Wedepohl, K., 1991. The composition of the upper earth's crust and the natural cycles of selected metals. Metal in natural raw materials, natural resources. Metals and their compounds in the environment. Occurrence, Analysis and Biological Relevance, 3–17.
Westerhold, T., Röhl, U., Wilkens, R.H., Gingerich, P.D., Clyde, W.C., Wing, S.L., Bowen, G.J., Kraus, M.J., 2018. Synchronizing early Eocene deep-sea and continental records–cyclostratigraphic age models for the Bighorn Basin Coring Project drill cores. Clim. Past 14, 303–319.
Wu, Q., Cui, Y., Wang, Y., Jiang, S., Dong, Y., Shen, J., 2024. Biogeochemical responses to global warming during the Paleocene–Eocene Thermal Maximum in the eastern Tethys. Palaeogeogr. Palaeoclimatol. Palaeoecol. 636, 111969.
Xi, D., Cao, W., Cheng, Y., Jiang, T., Jia, J., Li, Y., Wan, X., 2016. Late cretaceous biostratigraphy and sea-level change in the Southwest Tarim Basin. Palaeogeogr. Palaeoclimatol. Palaeoecol. 441, 516–527.
Xue, P., Chang, L., Thomas, E., 2023. Abrupt Northwest Atlantic deep-sea oxygenation decline preceded the Palaeocene-Eocene thermal Maximum. Earth Planet. Sci. Lett. 618, 118304.
Yang, J., Cawood, P.A., Montañez, I.P., Condon, D.J., Du, Y., Yan, J.-X., Yan, S., Yuan, D., 2020. Enhanced continental weathering and large igneous province induced climate warming at the Permo-Carboniferous transition. Earth Planet. Sci. Lett. 534, 116074.

Yang, S., Hu, W., Fan, J., Deng, Y., 2022. New geochemical identification fingerprints of volcanism during the Ordovician-Silurian transition and its implications for biological and environmental evolution. Earth Sci. Rev. 228, 104016.
Young, G.M., Nesbitt, H.W., 1998. Processes controlling the distribution of Ti and Al in weathering profiles, siliciclastic sediments and sedimentary rocks. J. Sediment. Res. 68, 448–455.
Zachos, J.C., Röhl, U., Schellenberg, S.A., Sluijs, A., Hodell, D.A., Kelly, D.C., Thomas, E., Nicolo, M., Raffi, I., Lourens, L.J., 2005. Rapid acidification of the ocean during the Paleocene-Eocene thermal maximum. Science 308, 1611–1615.
Zhang, S., Hu, X., Han, Z., Li, J., Garzanti, E., 2018. Climatic and tectonic controls on Cretaceous-Palaeogene Sea-level changes recorded in the Tarim epicontinental sea. Palaeogeogr. Palaeoclimatol. Palaeoecol. 501, 92–110.
Zhang, S., Hu, X., Garzanti, E., 2019. Paleocene initial indentation and early growth of the Pamir as recorded in the western Tarim Basin. Tectonophysics 772, 228207.
Zhang, X., Li, X.-L., Garzanti, E., Lin, C.-M., Deng, K., 2021. Sedimentary geochemistry response to climate change on a millennial timescale in the Qiantang River incised-valley system, eastern China. Chem. Geol. 586, 120587.
Zhou, L., Friis, H., Poulsen, M.L.K., 2015. Geochemical evaluation of the late Paleocene and early Eocene shales in Siri Canyon, Danish-Norwegian basin. Mar. Pet. Geol. 61, 111–122.